



Initiation and short crack growth behaviour of environmentally induced cracks in AA5083 H131 investigated across time and length scales

DOI:

[10.1515/correv-2019-0044](https://doi.org/10.1515/correv-2019-0044)

[Link to publication record in Manchester Research Explorer](#)

Citation for published version (APA):

Gudla, V. C., Garner, A., Storm, M., Gajjar, P., Carr, J., Palmer, B. C., Lewandowski, J. J., Withers, P. J., Holroyd, N. J. H., & Burnett, T. L. (2019). Initiation and short crack growth behaviour of environmentally induced cracks in AA5083 H131 investigated across time and length scales. *Corrosion Reviews*. <https://doi.org/10.1515/correv-2019-0044>

Published in:

Corrosion Reviews

Citing this paper

Please note that where the full-text provided on Manchester Research Explorer is the Author Accepted Manuscript or Proof version this may differ from the final Published version. If citing, it is advised that you check and use the publisher's definitive version.

General rights

Copyright and moral rights for the publications made accessible in the Research Explorer are retained by the authors and/or other copyright owners and it is a condition of accessing publications that users recognise and abide by the legal requirements associated with these rights.

Takedown policy

If you believe that this document breaches copyright please refer to the University of Manchester's Takedown Procedures [<http://man.ac.uk/04Y6Bo>] or contact openresearch@manchester.ac.uk providing relevant details, so we can investigate your claim.



Initiation and short crack growth behaviour of environmentally induced cracks in AA5083 H131 investigated across time and length scales

V C Gudla¹, A Garner¹, M Storm², P Gajjar¹, J Carr¹, B C Palmer³, J J Lewandowski³, P J Withers¹, N J H Holroyd¹, T L Burnett^{1*}

¹ Henry Royce Institute, School of Materials, The University of Manchester, Manchester, Lancashire, M13 9PL, United Kingdom.

² Diamond Light Source Ltd, Diamond House, Harwell Science and Innovation Campus, Didcot, Oxfordshire, OX11 0DE, United Kingdom

³ Department of Materials Science & Engineering, Case Western Reserve University, Cleveland, Ohio, 44106, USA

*corresponding author – timothy.burnett@manchester.ac.uk

Abstract

Environmentally induced cracking (EIC) in a sensitized high strength AA5083 H131 alloy has been investigated using time-lapse synchrotron X-ray computed tomography combined with post mortem correlative characterization. Small corrosion features deliberately introduced in a pre-exposure step were found to be the site of initiation for over 95% of the 44 EIC cracks that developed under slow strain rate testing. Detailed analysis using 3D electron back scatter diffraction (EBSD) and energy dispersive spectroscopy (EDS) analysis of a single crack confirmed the intergranular nature of the cracks from the start and that the pre-exposure corrosion was associated with an α -AlFeMnSi particle cluster. It also appears that several cracks may have initiated at this site which later coalesced to form the 300 μ m long crack that ultimately developed. Of further note is the fact that initiation of the EIC cracks across the sample started below the yield strength and continued beyond the ultimate tensile strength. The most rapid crack propagation occurred during sample extension following a period of fixed displacement.

Key words: 4D, humid air, EIC, non-propagating cracks, hydrogen embrittlement, correlative tomography

1. Introduction

Aluminium alloys based on the Al-Mg alloy system are widely used in marine applications owing to their high strength, low density, and good corrosion resistance to saline environments (Vargel, 2004)(Polmear, 2006). However, structural integrity issues pertaining to the AA5083 Al-Mg alloy used in marine service environments have called for further understanding of the environmental induced cracking (EIC) phenomenon of these material systems (Bushfield *et al.*, 2003). The EIC in structural components was attributed to high susceptibility to intergranular stress corrosion cracking (IGSCC) (Holroyd and Scamans, 2016). High strength AA5xxx alloys (> 3 wt.% Mg) rely on a combination of solid solution strengthening and cold working for their strength. These alloys are not precipitation hardenable, but do undergo ageing or precipitation at temperatures as low as 40 °C due to the low solubility of Mg in Al at room temperature (Scamans *et al.*, 1987)(Zhang *et al.*, 2016). The Mg-rich β -Al₃Mg₂ phase can form as a continuous or discontinuous layer along the grain boundaries and can severely compromise the corrosion and SCC resistance of these alloys as it is highly anodic with respect to the matrix (Davenport *et al.*, 2006)(Searles *et al.*, 2001)(Yang and Allen, 2013)(Goswami and Holtz, 2013)(Dix *et al.*, 1959). Intergranular corrosion (IGC), and IGSCC are both promoted by dissolution of the anodic β phase, leading to acidification of the crack tip/corrosion feature and generating H which is taken up by the surrounding Al which under an applied stress is believed to create the conditions needed to initiate IGSCC (Crane *et al.*, 2016)(Jones *et al.*, 2004)(Crane and Gangloff, 2016).

There is extensive literature on the effect of various parameters, including the composition, microstructure (Seifi *et al.*, 2015), inhomogeneity (Gao *et al.*, 2018)(Gao *et al.*, 2019), testing conditions (Brosi and Lewandowski, 2010)(Brosi *et al.*, 2012), degree of sensitization (DoS; a measure of susceptibility to IGC) (Jones *et al.*, 2001), and the pre-exposure

state (surface nature, corrosion pits and defects (Seong *et al.*, 2015), local stress raisers (Holroyd *et al.*, 2017a)(Holroyd *et al.*, 2017b), hydrogen content (Gupta *et al.*, 2016b), remediation treatments (Seifi *et al.*, 2018) etc.) of the material with respect to their IGC and IGSCC behaviour. Nevertheless a mechanistic understanding of crack initiation, propagation, and final failure is still incomplete (Holroyd and Scamans, 2016)(WEARMOUTH *et al.*, 1973)(Holroyd *et al.*, 2015)(Jones and Danielson, 2003)(Jones, 2003). One reason for this is that only recently have the tools become available to observe these phenomenon at relevant time and length scales. In order to engineer materials that provide EIC resistance, it is important to understand the propensity for crack initiation under particular combinations of environment and mechanical driving force as well as requirements and behaviour during propagation. In simple terms, reducing the probability of EIC initiation should reduce the likelihood of failure for any given time period. Staehle *et al.* (Staehle, 2011) classifies SCC initiation and propagation into five mechanistically different stages: the *initial condition* of the material surface; formation of *precursors* such as corrosion pits; *incubation* of SCC by hydrogen entry, grain boundary dissolution etc. to create the conditions needed for cracking e.g. suitable environment and concentrated stress; development of *proto-cracks* which are SCC cracks but sufficiently short that many of them ‘die’ early in life and finally *propagation* to failure (this could also describe as ‘sustained propagation’). Traditionally, the engineering definition for transition from initiation to propagation for nuclear energy applications is pinned at a crack length of 1.3 mm, and at around 3 mm for aerospace (Turnbull, 2017). This is defined as the depth of penetration of a crack beyond which the crack would start interacting with residual or/and applied stress fields within the material and is measurable via non-destructive inspection methods applied in service i.e. the minimum detectable feature.

Though these stages were proposed in the context of SCC of materials in nuclear energy applications, it can be extended more widely to SCC and EIC in other materials including high

strength Al-Mg alloys. To study and understand the nature of each of these stages, and to effectively link microscale phenomenon with the macroscale performance, multiscale time lapse studies are required. Over the past decade, several reports have been presented on corrosion (Vallabhaneni *et al.*, 2018), corrosion fatigue (Singh *et al.*, 2016a)(Stannard *et al.*, 2018), and EIC (Holroyd *et al.*, 2017a)(Burnett *et al.*, 2015)(Singh *et al.*, 2014) processes that have been studied non-invasively and non-destructively using X-ray radiography (Zhao *et al.*, 2003)(Liu *et al.*, 2006a)(Liu *et al.*, 2006b)(Liu *et al.*, 2007), and X-ray computed tomography (XCT) techniques (Eckermann *et al.*, 2009)(Eckermann *et al.*, 2008)(Turnbull, 2014)(Bradley *et al.*, 2017)(Knight *et al.*, 2011)(Singh *et al.*, 2016b)(Knight *et al.*, 2010)(Connolly *et al.*, 2006)(Gupta *et al.*, 2016a)(Carter *et al.*, 2018)(Horner *et al.*, 2011). Burnett *et al.*, have demonstrated how lab-based XCT can be used to understand the 3D morphology of environmental induced cracks (Holroyd *et al.*, 2017a)(Burnett *et al.*, 2015). In addition, the exceptional flux available at synchrotron X-ray sources allows for the electrochemically and mechanically driven events occurring during EIC to be studied in real time (Singh *et al.*, 2017)(Singh *et al.*, 2016c)(Henthorne, 2016)(Singh *et al.*, 2016d).

In this paper a correlative XCT approach (Burnett *et al.*, 2016)(Burnett *et al.*, 2014)(Burnett *et al.*, 2017)(Slater *et al.*, 2017) combining time-lapse synchrotron XCT during slow strain rate testing (SSRT) followed by site-specific post-mortem analysis was performed to study the EIC initiation and propagation to failure of an AA5083 H131 alloy.

2. Experimental

2.1. Materials

Commercially available H131 temper AA5083 alloy plates of 29 mm thickness having the composition summarised in Table 1 were used in this study. The composition of the as-

received plates was measured using optical emission spectroscopy. The susceptibility to IGC was evaluated using the Nitric Acid Mass Loss Test (NAMLT) according to ASTM G67 (ASTM, 2013). The Degree of Sensitization (DoS) value obtained for the as-received samples was 8.6 mg/cm² (Holroyd *et al.*, 2017a). The as-received material had typical pancake-shaped elongated grains along the rolling direction and with an average length (L) of 150 μm, and widths of 35 μm (S) and 80 μm (T). The measured short transverse tensile yield stress (YS), ultimate tensile stress (UTS) and plane-strain fracture-toughness (KIC) properties were 260 MPa, 375 MPa, and 31 MNm^{-3/2} respectively (Seifi *et al.*, 2016).

Table 1: Composition of the as-received AA5083 H131 plates (in wt.%).

Mg	Mn	Fe	Cr	Si	Zn	Ti	Ni	Sn	Pb	Al
4.46	0.62	0.12	0.08	0.07	0.02	0.02	<0.01	<0.01	0.01	Bal.

Cylindrical tensile test samples of 12.7 mm gauge length and 3.2 mm diameter were machined in the short-transverse orientation from the as-received plates for SSRT (Seifi *et al.*, 2016). The samples were then mechanically polished using SiC abrasive grinding paper of P4000 grade, and then ultrasonically cleaned with ethanol followed by warm air drying. In order to enhance the susceptibility of the as-received samples to IGC, an additional sensitization treatment was performed at 80 °C for 225 h. This resulted in an increase of DoS (NAMLT value) to ~40 mg/cm². The sensitized samples were further subjected to pre-exposure in a 0.6 M NaCl solution at RT for a period of 180 h in order to introduce surface corrosion attack e.g. IGC, as well as charging the sample with hydrogen. The surface corrosion features are expected to act as realistic stress raising sites during SSRT (Holroyd *et al.*, 2017a). Following pre-exposure, the gauge lengths of tensile specimens were rinsed, carefully dried and immediately subjected to SSRT. The regions of the sample gauge length on either side of the central region were masked with Parafilm™ (Bemis Company, Inc). This helped to prevent

failure in the shoulder region of the SSRT samples and also provided a window of environmental exposure commensurate with the field of view (FOV) of the X-ray imaging.

2.2. Slow strain rate testing

SSRT of the samples were performed at a nominal strain rate of $4 \times 10^{-5} \text{ s}^{-1}$ using a Deben CT5000 5 kN mechanical test rig (CT5000 5KN in-situ tensile stage for μ XCT applications | Deben UK – the microscopy accessory experts, n.d.). The test was performed by straining the sample up to UTS at this strain rate, after which the displacement was fixed to provide constant strain until final failure of the sample occurred. Within the constant strain rate regime of the SSRT prior to achieving UTS, the straining was paused intermittently to allow XCT data acquisition taking ~ 90 s to avoid image blurring. This results in a stepwise increment in the applied load on the sample. A humid atmosphere around the sample during testing was achieved by placing wet sponges at the base (~ 20 mm away from the sample gauge length) of the vitreous glassy carbon test chamber giving a humidity level of $\sim 70\%$ RH at RT and minimising X-ray absorption.

2.3. Synchrotron 3D XCT

Synchrotron XCT was conducted at the I13-2 imaging beamline at Diamond Light Source, UK. A ‘pink beam’ (Rivers, 2016) was used for imaging to maximize the flux around a nominal energy of 28 keV. The detector provided a 4.2 mm x 3.5 mm field of view with a $(1.63 \mu\text{m})^3$ voxel size. The exposure time was 0.035 s for each of the 1200 projections totalling up to ~ 90 s per tomogram acquisition. A total of 43 tomograms were collected in-situ over a period of 13260 s (3 h, 41 min) of testing in addition to those collected prior to and after testing. After an initial low noise XCT scan with a 0.09 s exposure time, scans were collected at regular intervals until the yield strength was exceeded and then recorded continuously once the UTS was reached. Further, an additional tomogram with an exposure time of 0.09 s was acquired

after testing. Reconstruction was performed using the Gridrec algorithm (Dowd *et al.*, 1999) of the TomoPy software (Gürsoy *et al.*, 2014) module within a Savu pipeline (TomoPy — TomoPy 1.1.3 documentation, n.d.).

2.4. Analysis Methodology

Avizo™ software (ThermoFisher Scientific (Thermo Fisher Scientific, 2018)) was employed to visualise and analyse the reconstructed XCT data. The data from the time step just prior to failure was first utilized to identify the full extent of cracking that had developed during SSRT within the field of view. The individual cracks were then numbered and tracked back through the time sequence using the time-lapse tomograms to identify the location and time step of origin. The point of initiation in time was identified by checking for the presence of the crack in a specific tomogram, and confirmed only if it was measurable to at least 3 voxels in dimension, i.e. at least 5 μm and clearly visible as a change from the previous time-step. The temporal resolution of identifying the time of initiation is limited in accuracy by the time elapsed between the two tomograms in which the crack had initiated and was large enough to be confidently measured. The crack length was always measured as the depth which the crack penetrates radially inwards towards the sample centre from the surface initiation site. Topographical features of the crack (i.e. variations in height) are excluded in these measurements as the cracks are generally very flat. The length of all the identified cracks was measured for each of the collected tomograms. This measurement protocol for crack lengths was semi-automated using the scripting capability within the Avizo™ software module.

2.5. Post-mortem characterization

The morphology of the fracture surface of the sample after SSRT was investigated using an FEI Quanta 650 field emission gun scanning electron microscope (FEG-SEM) coupled with an energy dispersive X-ray spectroscopy capability. Through correlation with the XCT data, a

specific crack was identified in the SEM for further examination using focused ion beam (FIB-SEM) serial section tomography. The volume of interest for this analysis was chosen from the XCT data volume rendering and was identified in the SEM by correlating the corresponding surface corrosion features and distance from the fracture surface on the sample gauge length. A volume with approximate dimensions $175 \times 175 \times 200 \mu\text{m}^3$ containing the majority of the EIC crack of interest was lifted out using an FEI Helios Xe^+ Plasma Focused ion beam (PFIB), further details of this technique can be found elsewhere (Burnett *et al.*, 2017)(Slater *et al.*, 2017)(Gillen *et al.*, 2018). After extraction, the block was attached to a Cu transmission electron microscopy (TEM) grid. The grid holding the block was subsequently mounted onto a pre-tilted holder and serial sectioning was performed using the PFIB operated at 30 keV with a current of 59 nA with FEI Auto Slice and View 4 software. The slice thickness was chosen to be 300 nm in order to capture the finer details of the crack path and to enable chemical mapping of small precipitates, a rocking mill of 9° was also used to reduce curtaining effects during milling which can be exaggerated by the presence of the crack in the milling direction. After each slice, simultaneous EBSD and EDS acquisitions were performed with a step size of 250 nm using the electron beam operated at 20 keV and 22 nA using Oxford Instruments Aztec software. In addition, at each slice, a secondary electron image was collected in order to image the crack path and correlate to the crystallographic and chemical data. The total volume of analysed material was $175 \times 175 \times 80 \mu\text{m}^3$ captured in ~300 slices.

3. Results and Discussion

3.1. SSRT

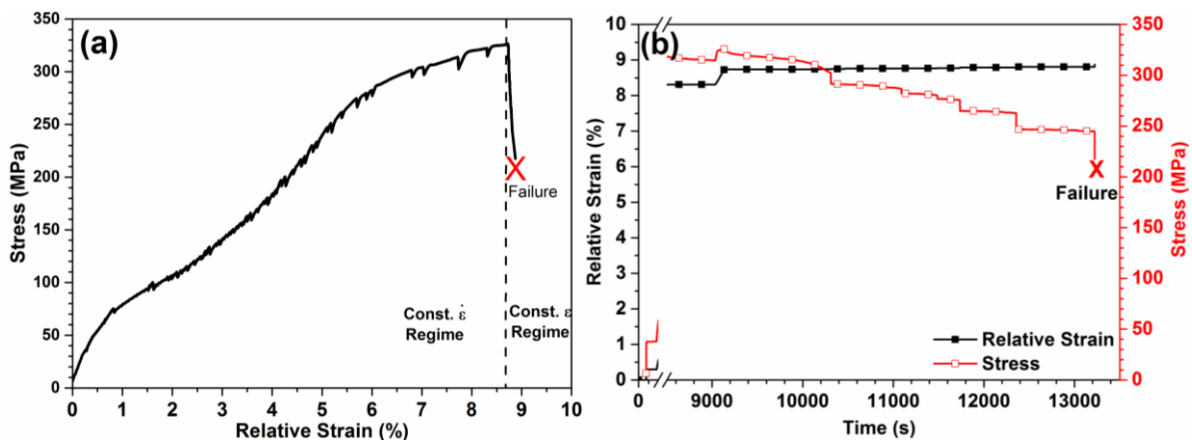


Figure 1: (a) Engineering Stress vs. relative strain response of the AA5083 sample, showing the region of switch from slow strain rate testing to fixed displacement testing, and the final failure. From 0 to ~3% relative strain, the plot displays a region showing the slack of the SSRT system; (b) Engineering stress and relative strain vs. test time showing the region of constant strain or fixed displacement highlighting the load drops observed until final failure.

The engineering stress vs. the relative strain from the SSRT of the sample tested is shown in Figure 1 (a). As can be seen, at around 325 MPa (close to UTS), the test was switched to constant strain or fixed displacement mode from the slow strain rate testing mode. Initially, the stress increases linearly with strain followed by yielding of the sample at ~275 MPa. After switching to fixed displacement mode at ~2.2% plastic strain, the stress across the sample drops from approx. 325 MPa to 225 MPa over a period of just over 4500 s as the EIC cracks grow leading to final failure. The stress vs. time during the fixed displacement regime of the SSRT is shown in Figure 1 (b). The drop in stress prior to failure was not immediate, but proceeded in a slow downward trend coupled with several small load drops.

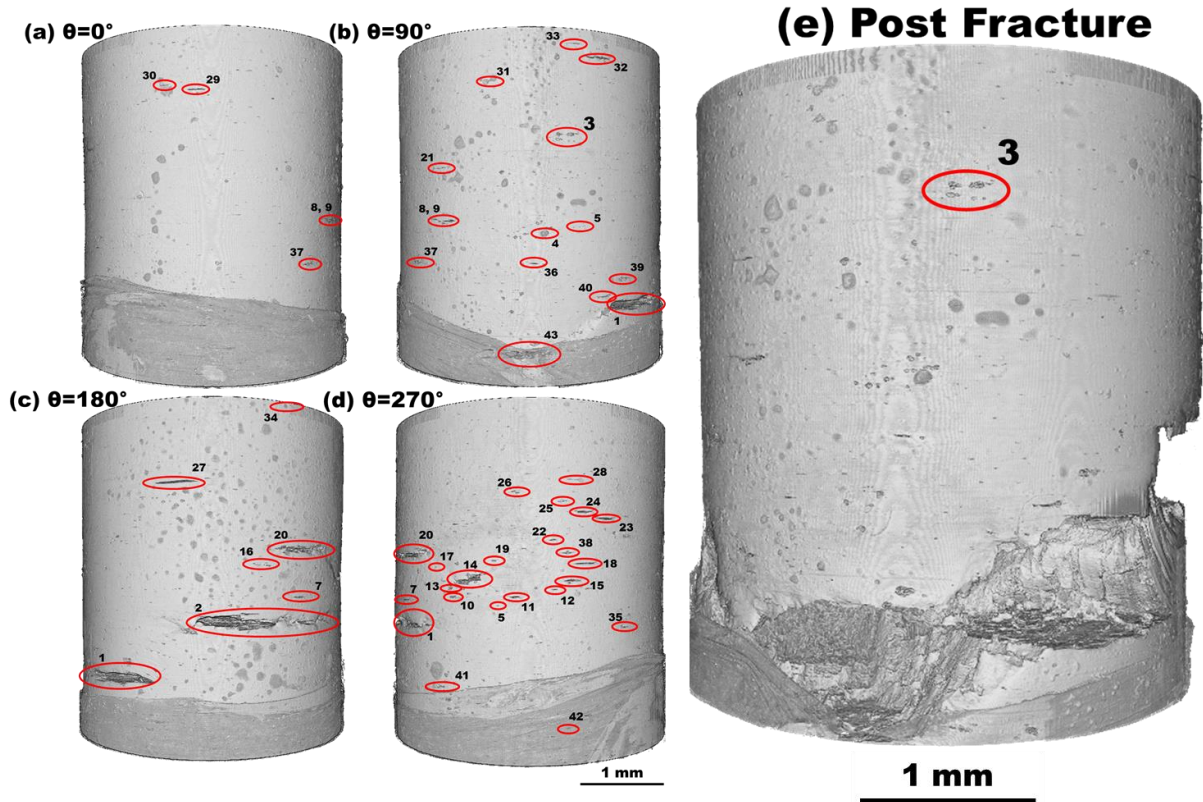


Figure 2: (a-d) Volume renderings of the gauge length of the sample at four different viewing angles (θ) obtained at a time step just prior to failure showing all the 44 EIC cracks that were numbered and investigated, and (e) volume rendering of the sample gauge length after failure showing the relative location of the specific EIC Crack marked “3” on the sample gauge length that was subject to further characterisation. The protective Parafilm™ used to prevent cracking outside the XCT field of view is also visible at the bottom end of the image.

Figure 2 (a)-(d) shows the sample just prior to failure and shows features such as the corrosion sites due to pre-exposure (covered by corrosion products in some locations) as well as the catalogued (numbered) EIC cracks, while the route of the final failure is shown in Figure 2 (e).

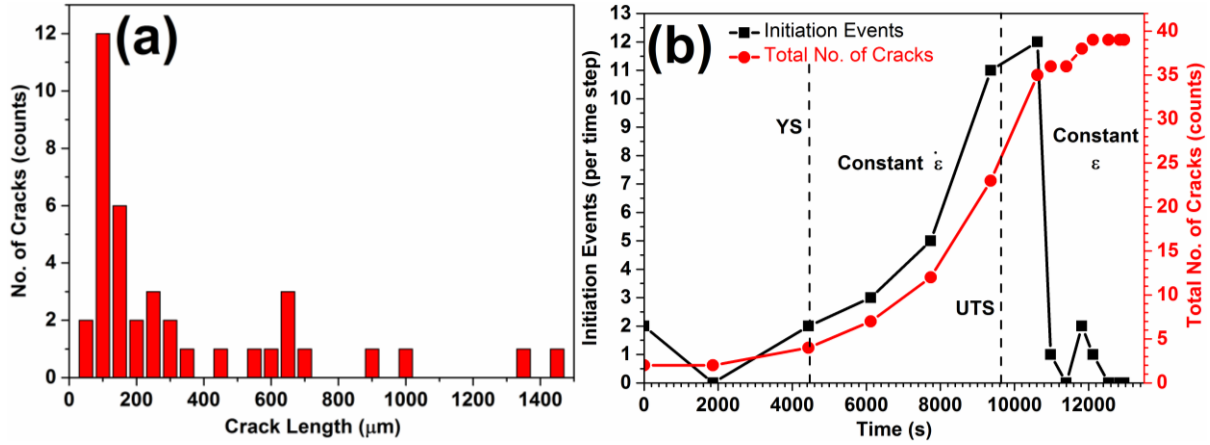


Figure 3: (a) Distribution of crack lengths in the sample measured from XCT data acquired just prior to overload failure (bin size = 50 μm), and (b) EIC Crack initiation events per time step, and total number of cracks as a function of test time (YS – Yield Stress, UTS – Ultimate Tensile Strength). All data measured from the reconstructed XCT images.

The number of EIC cracks measured from the XCT data acquired just prior to failure is shown in Figure 3 (a) as a function of the crack length. The engineering stress and plastic strain on the sample at this stage are ~ 245 MPa (post UTS) and $\sim 2.2\%$ respectively. The number of EIC crack initiation events, and the total number of cracks as a function of SSRT test time obtained from the time lapse XCT data is presented in Figure 3 (b). Crack initiation only starts at around 215 MPa (i.e. below yield), or after about 3700 s from the start of straining. The number of initiation events recorded gradually increases beyond yield point of the sample and drops sharply when the loading is changed to fixed displacement mode. Indeed, only four additional initiation events were observed after the switch to fixed displacement mode, although it is possible these cracks also initiated in the constant strain rate region and only grew large enough to be resolved by the XCT imaging slightly later. A total of 44 cracks were indexed and tracked through the test time and their size, location, and time of initiation were recorded within the spatial and temporal resolution limits. Of the 44 cracks that were indexed using the time-lapse XCT data, 5 minor cracks (< 50 μm), and 5 major cracks (> 50 μm , can

be identified on the fracture surface in Figure 4 (a)) contributed to the final failure. Further, it was found that of all the 44 cracks that were indexed, 42 of them initiated from a surface feature corresponding to intermetallic phases or corrosion sites based on the proximity to the associated crack.

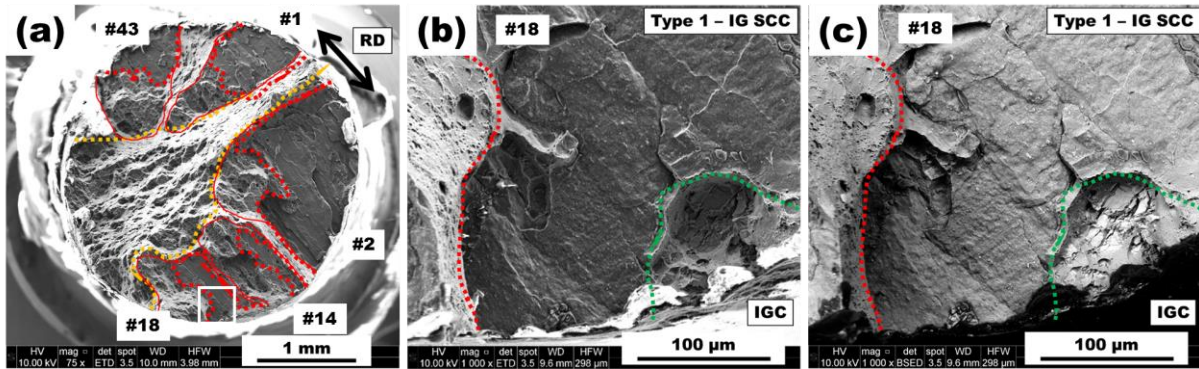


Figure 4: Secondary electron (SE) SEM images showing (a) overview of the fracture surface with IGSCC (Type 1, dotted red lines), Type 2 cracking (solid red lines), and multi-void coalescence (MVC, region within the dotted orange lines) along with the specific identified EAC crack numbers correlated from XCT data; (b) a closer look at the IGSCC (crack #18) fracture surface showing the region of initiation at a corrosion site (dotted green lines), and (c) Back scattered SEM image of region shown in (b) showing the bright appearing cluster of intermetallic phases at the surface corrosion site.

The fracture surface in Figure 4 (a) shows three major distinct regions displaying features corresponding to the IGSCC region (Type 1 fracture), Type 2 EIC, and micro-void coalescence (MVC) in addition to the surface corrosion sites. 35-40% of the fracture surface is identified as IGSCC which display a flat morphology which appears ‘shiny’ when viewed optically. Further, it is observed that the IGSCC regions are followed by Type 2 EIC cracking features characterized by their stepped topography and very large and shallow dimple-like features containing patches of particles (Holroyd *et al.*, 2017a). It is also observed that in all the instances, Type 2 EIC cracking is always preceded by Type 1 IGSCC. The total IGSCC area (Type 1) and Type 2 EIC area comprise approx. 60% of the fracture surface when viewed in plan view. The remaining 40% of the fracture surface is attributed to MVC that occurred

during the final stages of fast fracture and is characterized by the steep topography. Most of the IGSCC sites found on the fracture surface could be tracked back to features corresponding to surface corrosion sites. An example of this is presented in Figure 4 (b) (SE image) and (c) (corresponding BSE image) where a cluster of intermetallic particles (confirmed by SEM EDS to be AlFeMnSi based) at the surface of the sample gauge length have formed a corrosion site during the pre-exposure treatment in NaCl solution. This corrosion site is followed by IGSCC (Type 1 EIC cracking).

By considering the crack length vs. time data during the fixed displacement regime of testing, it was observed that the velocity of some of the cracks reduced. One such EIC crack belonging to this subset (crack 3), was investigated in further detail. This specific crack initiated in the constant strain rate part of the test at a stress value of approx. 215-245 MPa i.e. below the yield strength. The crack had a length of $\sim 258 \mu\text{m}$ (the 5th largest) when the fixed displacement testing began and appeared to be still growing (the global average length of all the cracks at this stage was approximately $80 \mu\text{m}$). At the end of the test, just prior to failure, the length of crack 3 increased by only 10% to $\sim 283 \mu\text{m}$ (11th largest overall) while the average crack length had increased by 250% (to $\sim 280 \mu\text{m}$). By comparison the longest crack had grown from $497 \mu\text{m}$ to $1447 \mu\text{m}$. As it is clear that this specific crack had grown considerably in the constant strain rate mode of the test, but almost stopped growing completely in the fixed displacement regime, it was of interest to investigate this crack further in detail to try and understand how it initiated and grew, and why it stopped. This crack also did not contribute to the final failure as seen in Figure 2.

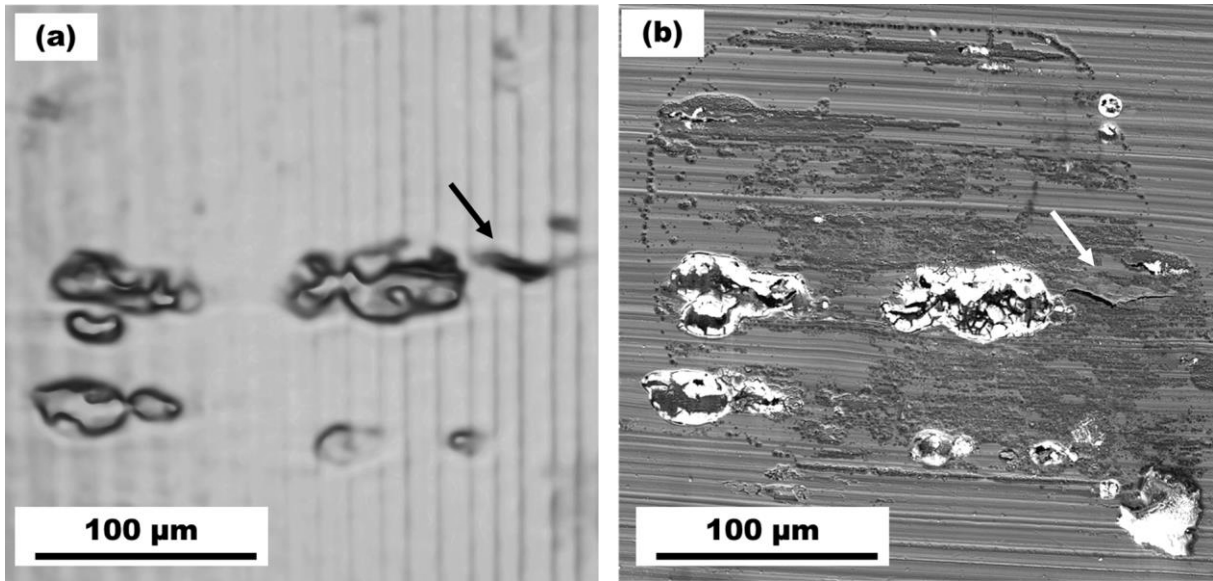


Figure 5: (a) Volume rendering of the sample gauge length surface obtained from the XCT data of the sample showing the region of interest where EIC Crack 3 (marked with black arrow) initiated, and (b) the corresponding SEM SE image of the surface showing the corrosion sites associated with intermetallic particles and the EIC Crack 3 (marked with white arrow) initiating from one of these sites.

Figure 5 shows the XCT surface rendering as well as the corresponding SE image of the corrosion site from where the crack 3 initiated. In Figure 5 (a), cracking can be seen to originate from the edge of one of the surface corrosion sites, which can be seen more clearly in the SE image in Figure 5 (b). Four distinct surface corrosion sites are visible. In addition, the SE image also shows corrosion products on the sample surface and general corrosion of the surrounding Al matrix, which is beyond the spatial resolution of the XCT images. EIC cracking can be clearly observed connecting to the edge of one of the corrosion site in the SE image in Figure 5 (b).

In order to better visualise the growth of the crack, the 3D XCT volume of the crack was segmented and visualised at various stages of the test as shown in Figure 6. It is clear that there were no major changes to the crack length and morphology under fixed displacement conditions, indicative of minimal EIC propagation for this crack.

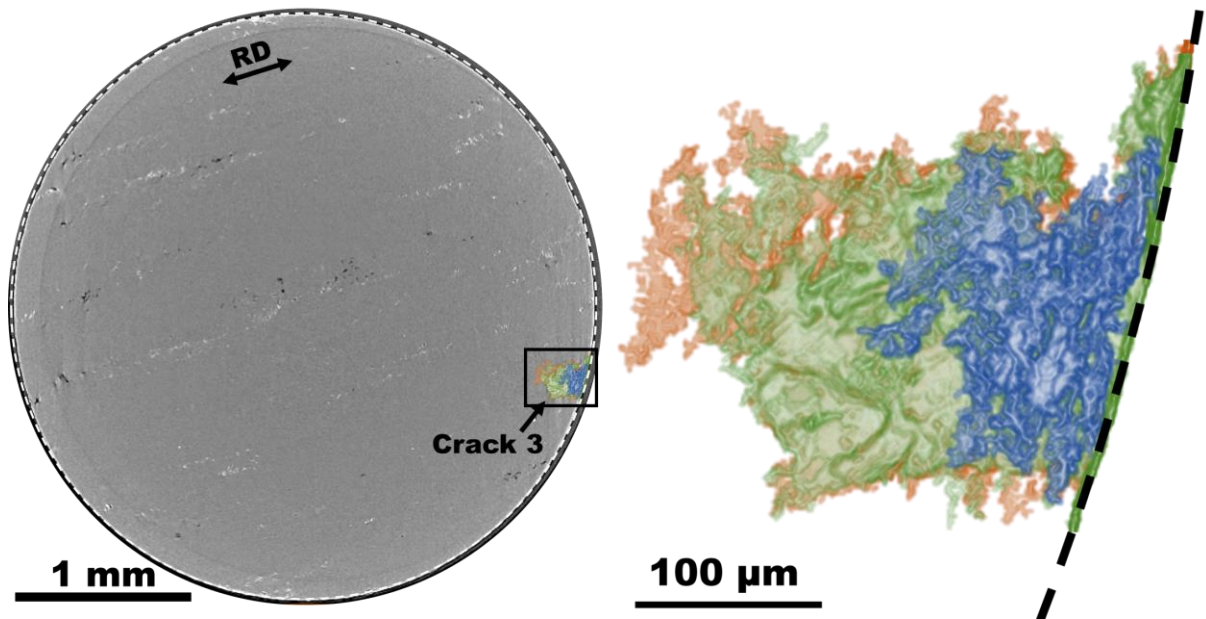
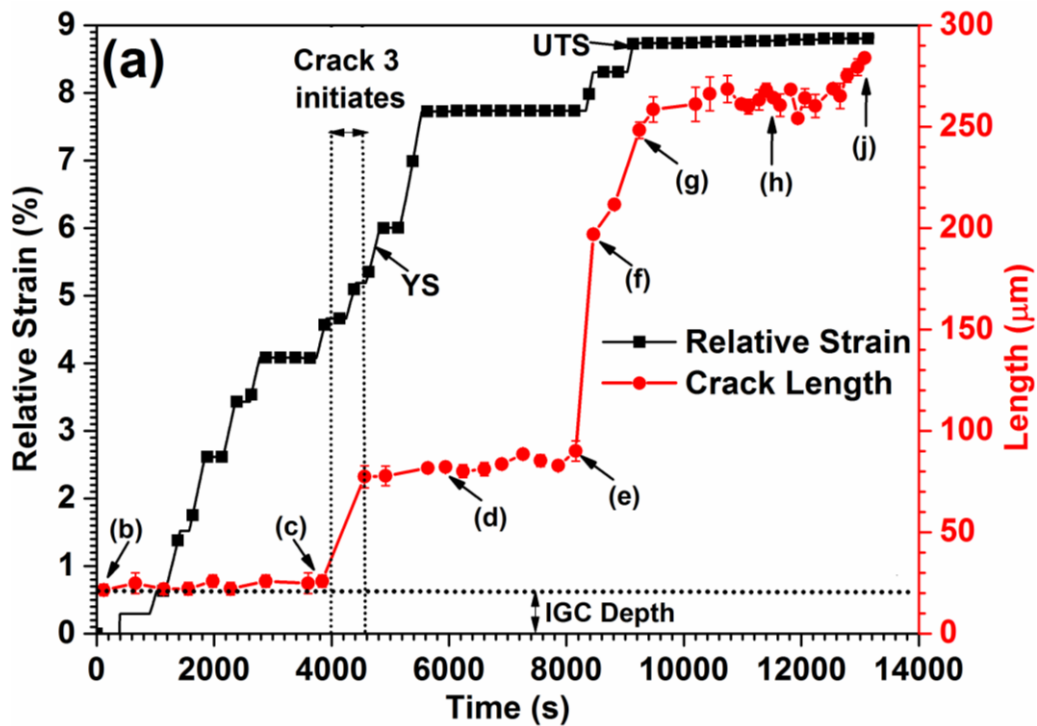


Figure 6: 3D volume renderings of the Crack 3 generated by segmenting the XCT data of the crack volume during slow strain rate testing (blue crack $t = 8460$ s) at the transition to constant displacement (green crack $t = 9480$ s) and after a period of constant displacement just before the final failure of the specimen (orange crack $t = 13080$ s).



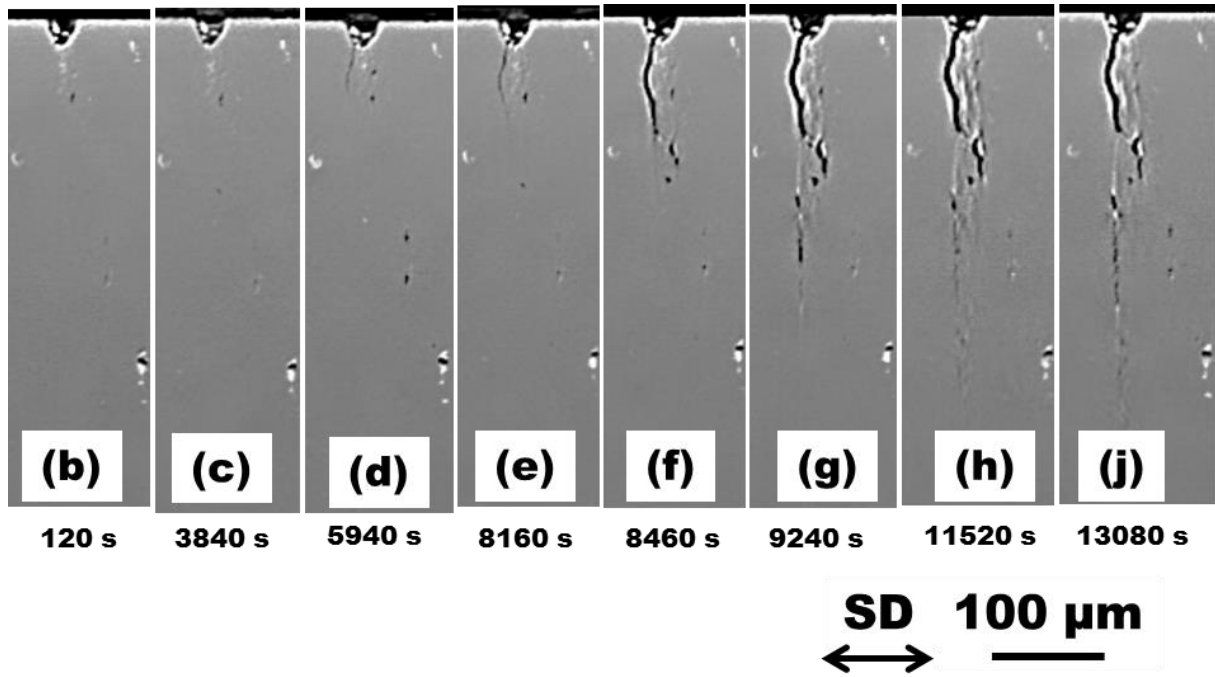


Figure 7: (a) Length of ‘crack 3’ measured from the time lapse XCT data, and calculated relative strain on the sample vs. test time showing - 0.2% Yield strength – 275 MPa, Initiation window of the crack 3, UTS – 325 MPa, and the initial IGC site depth; (b-j) XCT virtual slices of the sample showing the crack at various stages of the test marked in (a). SD – straining direction.

The crack length and the relative strain on the sample vs. the test time, are shown in Figure 7 in addition to selected XCT virtual slices of ‘crack 3’ shown at different time steps. The initiation of crack 3 occurred from a 30 μm feature (to be discussed later) between $t = 3800$ s - 4500 s (Figure 7). The crack appears to grow visibly in the early stages before growing quite abruptly. The virtual slices of the cross section of the crack from time lapse XCT data shown in Figure 7 (b)-(j) reveal the growth as well as the changes in path of the crack before appearing to become dormant in the fixed displacement regime. Lastly a small slow increment of growth is observed just before sample failure. The highly branched nature of the crack is observed in the Figure 7 (f)-(j). The stepwise increase in the strain is due to the intermittent loading of the sample that was employed prior to yielding to allow steady state conditions during XCT acquisition. Beyond a plastic strain value of ~2% ($t = \sim 5500$ s) the first instance of fixed

displacement was applied. During this period no crack growth was observed in the sample after over 1 hour, therefore it was decided that the load at fixed displacement was too low and displacement was increased in a further step (at $t = \sim 8000$ s). Following this, crack growth occurred registering both in the mechanical response of the sample and the raw 2D X-ray projections. In the subsequent analysis of the 3D data a rapid increase in the crack length is evident. A further increase in strain (at $t = \sim 9000$ s) was followed by another increase in crack length. This step-up in load was performed to allow growth of the crack under subsequent fixed displacement mode in a reasonable amount of test time. During the fixed displacement stage ($t > \sim 9000$ s) it is observed that the crack did not propagate for a period followed by a small, slow increment in length. The largest growth occurred during the reloading step at $t = \sim 8000$ s. In addition, most of the instances of change in length of the crack can be correlated to the change in strain on the sample due to applied load change. The implications of this method of testing will be discussed later.

Post-mortem characterization of 'crack 3' was conducted in order to better understand the interaction of this crack with the microstructure. EDS elemental and EBSD mapping were employed to relate the crack path to the local grain orientations and the nature of any local second phases. Selected SEM SE images, corresponding EDS O $K_{\alpha 1}$ maps and EBSD IPF Z maps from this analysis are presented in Figure 8.

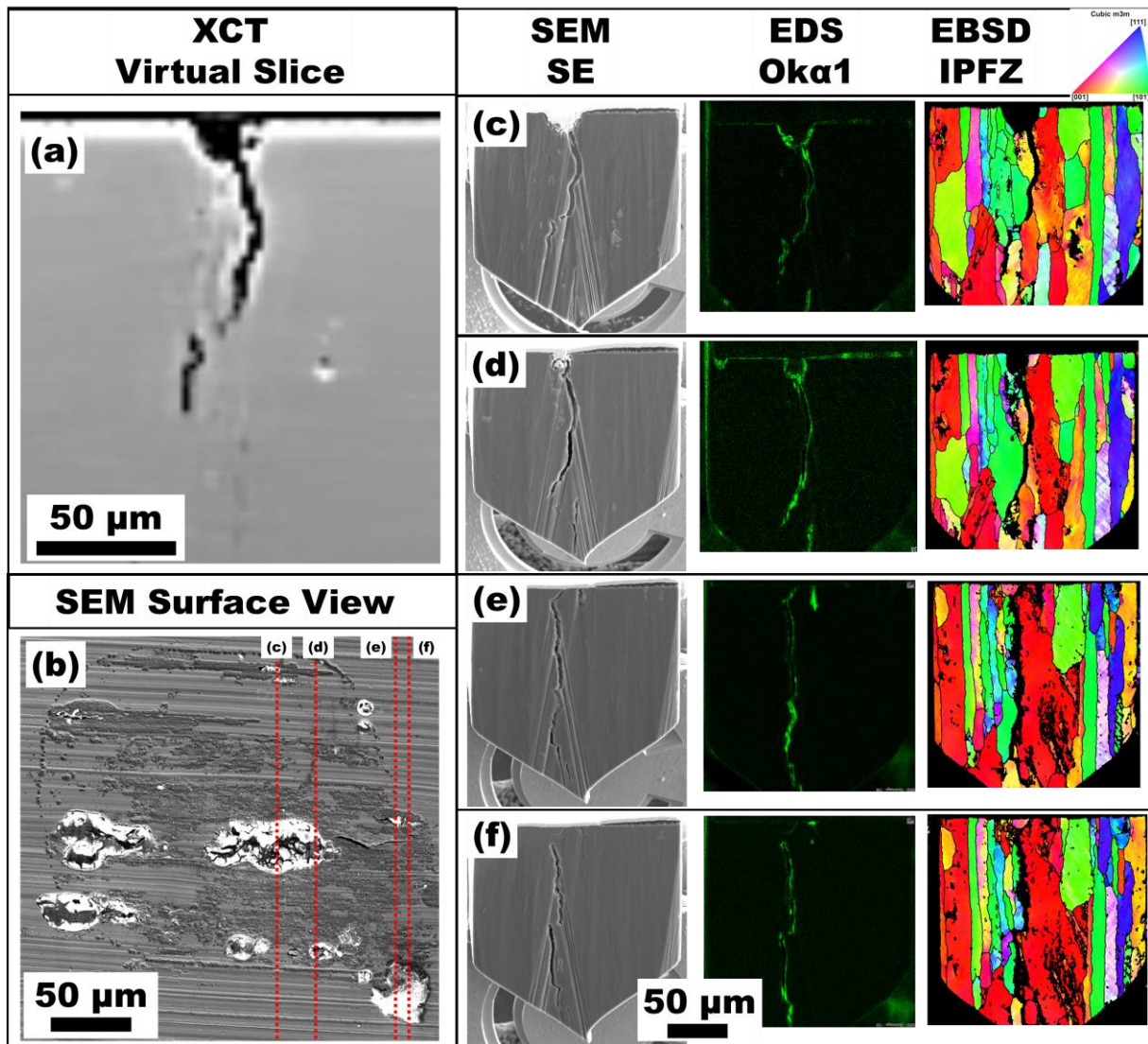


Figure 8: (a) XCT Virtual slice (filtered) showing initiation region and morphology of ‘crack 3’, (b) SEM SE surface view of the corrosion site from where the crack initiated showing the locations (marked in red) of the presented PFIB cross-sections (c)-(f) from which SE images, EDX and EBSD maps were acquired. Slice (c) corresponds to the XCT virtual slice in (a)

The local microstructure and chemistry of the region neighbouring ‘crack 3’ is shown in Figure 8 via 4 PFIB sections. The SEM SE images in Figure 8 (c) and (d) appear to show the crack originating from the bottom of the corrosion site, while that in Figure 8 (e) shows that the crack has followed a grain boundary which is at a $\sim 45^\circ$ angle to the surface. Some of the sharp changes of direction of the crack near the surface were initially thought to be tears through ligaments between different crack regions. However, the corresponding EBSD

orientation maps show that in all instances the crack is propagating along grain boundaries, as expected due to the IGSCC or Type 1 nature of EIC. Close to the initiation site, the crack path is more tortuous as it follows the grain boundaries, but as the crack develops it becomes more planar as it follows the boundary of the large (red) grain that extends almost throughout the entire volume to the right of the crack in Figure 8 (e) and (f). It appears that this large grain leads an interconnected high angle grain boundary with a number of neighbouring grains across the entire 3D volume, providing a direct route for crack propagation in the most mechanically favourable direction. The highly disjointed nature of these first increments of crack growth and the fact that the further along the length of the crack (deeper into the material) the crack opens up, leads us to believe that several very small cracks originally initiated from the particle cluster. It is surmised that with further growth these small cracks then coalesced leading to the opening of the crack and continuation as a single larger crack.

A total of 11 grain boundaries were analysed across these slices, out of which 10 are observed to be high angle grain boundaries (misorientations ranging from 23 - 53°). However, one cracked grain boundary was observed to be a low angle boundary (~8° misorientation) despite the fact that low angle grain boundaries (misorientation <15°) are generally considered as resistant to intergranular attack (Davenport *et al.*, 2006)(Seifi *et al.*, 2015)(Yuan *et al.*, 2001)(Tan and Allen, 2010)(Scotto D'Antuono *et al.*, 2014). Post-mortem analyses in other work (Seifi *et al.*, 2015) also showed a propensity for EAC along high angle grain boundaries in sensitized Al-Mg. The susceptibility of particular boundaries to attack can also be related to the propensity to induce β -phase precipitation, which determines whether precipitation along boundaries is continuous or discontinuous (Davenport *et al.*, 2006). However it was not possible to resolve any β -phase at grain boundaries during the serial sectioning experiment due to their estimated small size (~<50 nm) (Scotto D'Antuono *et al.*, 2014).

The observations made from the 3D volume renderings and the subsequent SEM characterization show that the pre-exposure treatment in NaCl solution has resulted in corrosion of the surface of the AA5083 sample. This material is known to contain phases such as α -AlFeMnSi and Mg₂Si in addition to β -Al₃Mg₂. Localised corrosion is focused around these particles resulting in pitting or IGC (Oguocha *et al.*, 2008). The α -AlFeMnSi phases are cathodic or electrochemically less active compared to the Al matrix, while the Mg₂Si and β -Al₃Mg₂ are anodic or electrochemically more active to the surrounding Al matrix (Buchheit, 1995)(Birbilis and Buchheit, 2005). The cathodic intermetallic phases support the cathodic reactions and lead to anodic dissolution of the surrounding matrix, leading to trenching and in some cases fall out of the intermetallic phase due to mechanical debonding. On the other hand, the anodic intermetallic phases in this material preferentially dissolve and cause pitting in the Al matrix, and if present at GBs lead to preferential GB dissolution and intergranular attack. In the current investigation, most of the corrosion sites resolved on the sample surface could be identified to be associated with the cathodic intermetallic phases and as mentioned earlier, 42 of the 44 EIC cracks initiated at these features, which are clearly visible as bright particles connected to the crack at the sample surface. As well as being active corrosion sites it is clear that these sites are creating the conditions to initiate EIC cracks. Although it is only during the subsequent exposure to the stress and humid air that these cracks actually initiate and start growing.

The observations from the PFIB cross-sections of Crack 3 show that this specific crack may have originated at the bottom of the corrosion site associated with the cathodic intermetallic phases, or at the surface next to this corrosion site at the GB as seen in Figure 8 (e). Within the spatial and temporal resolution of the current XCT acquisition parameters, it is however not possible to determine at which location cracking first started. However, considering the sensitization treatment performed to the samples, the presence of β -Al₃Mg₂

phase is expected at grain boundaries (Zhang *et al.*, 2016)(Searles *et al.*, 2001)(Seifi *et al.*, 2016)(Birbilis *et al.*, 2013) which in the vicinity of the α -AlFeMnSi intermetallic phases in the corrosion site is expected to cause galvanic coupling further enhancing corrosion propagation at the adjacent grain boundaries under humid conditions. This, under applied external load, leads to Type 1 EIC cracking. Further, studies performed on environmentally assisted fatigue crack propagation show that in majority of the instances, in presence of a corrosion pit, EIC initiation occurs at the edge of the corrosion site on the surface of the sample and not at the bottom of the corrosion site (Turnbull, 2017). This is postulated to be due to the local increase in strain and also easier availability of oxygen from the atmosphere close to the sample surface, than at the bottom of the corrosion site. In short, the easy access to oxygen, combined with the enhanced galvanic coupling between the cathodic α -AlFeMnSi particles and the anodic β -Al₃Mg₂ provide a high probability for EIC initiation. In view of this, it seems most likely that this specific EIC crack, though observed to have originated from the bottom of the corrosion site from the XCT data resolution limits, could have actually initiated from the edge of the corrosion site on the sample surface and then propagated inwards as seen in Figure 8 (Turnbull, 2017) to run along the entire outside edge of the intermetallic corrosion site. Once, one or more such EIC cracks have initiated (i.e. proto-cracks. (Staehele, 2011)), they can grow and coalesce thus providing sufficient length and driving force for the crack to enter the sustained propagation stage.

In summary, the pre-exposure of the sample has created small corrosion sites which provide preferential sites for EIC nucleation. Initiation starts below the yield strength and continues past the UTS but abruptly stops when constant strain *rate* switches to fixed displacement. However growth of a single crack analysed in detail propagates at the highest velocity when the loading regime changes back from fixed displacement to constant strain *rate*. Detailed analysis of a single crack revealed the site of initiation to be a α -AlFeMnSi particle

cluster from which it appeared several small proto-cracks emerged which later coalesced to form a single crack which then propagated to around 300 μm in length.

4. Conclusions

Monitoring of the initiation and growth of EIC has been undertaken by time-lapse synchrotron X-ray CT along with correlative PFIB-SEM serial sectioning to look at the local microstructure of a specific crack. These experiments have revealed that

- EIC sites were almost exclusively (>95%) associated with corrosion sites generated during pre-exposure ahead of straining and arguably directly related to the regions associated with the $\alpha\text{-AlFeMnSi}$ particles.
- 85% of the EIC cracks initiated under constant strain rate conditions between 95% of the yield stress and the ultimate tensile stress (325 MPa).
- The cracks propagate intergranularly and show evidence of crack branching.
- A single crack ('Crack 3') was studied in detail and despite initiating first and propagating at one of the highest rates under constant strain rate regime, it stopped when fixed displacement was applied. It grew most rapidly as extension was imposed on the sample again after a dwell under fixed displacement.
- The nature of initiation was found to be complex. It appears that multiple proto-cracks may have emerged from a single corrosion site and then coalesced as short cracks before they continued to grow.

Acknowledgements

V.C.G, P.G, J.C, T.L.B. and P.J.W. are grateful to funding from the ERC under grant CORREL-CT No. 695638. The experimental facilities in the Henry Royce Institute for Advanced Materials established through EPSRC funding for Henry Moseley X-ray Imaging Facility under grant Nos. EP/M010619, EP/K004530, EP/F007906, EP/F001452, EP/I02249X, EP/F028431 is acknowledged in addition to HEFCE funding through the UK Research Partnership Investment Funding (UKRPIF) Manchester RPIF Round 2 for the Multiscale Characterisation Facility. Additional support has been provided by the Arthur P. Armington Professorship (J.J.L.) and ONR-N00014-17-1-2573. Supply of materials was from Alcoa Technical Centre. This work was carried out with the support of the Diamond Light Source, instrument I13 (proposal MT18165-1).

References

- ASTM. (2013) ASTM G67-13 Standard Test Method for Determining the Susceptibility to Intergranular Corrosion of 5XXX Series Aluminum Alloys by Mass Loss After Exposure to Nitric Acid (NAML T Test). ASTM International, West Conshohocken, PA. *Annual Book of ASTM Standards*. <<https://doi-org.proxy.findit.dtu.dk/10.1520/G0067-13>>.
- Birbilis, N. and Buchheit, R.G. (2005) Electrochemical Characteristics of Intermetallic Phases in Aluminum Alloys: An Experimental Survey and Discussion. *Journal of The Electrochemical Society*, **152**, B140–B151.
- Birbilis, N., Zhang, R., Lim, M.L.C., Gupta, R.K., Davies, C.H.J., Lynch, S.P., Kelly, R.G. and Scully, J.R. (2013) Quantification of sensitization in AA5083-H131 via imaging gas-embrittled fracture surfaces. *Corrosion*, **69**, 396–402.

- Bradley, R.S., Liu, Y., Burnett, T.L., Zhou, X., Lyon, S.B., Withers, P.J., Gholinia, A., Hashimoto, T., Graham, D., Gibbon, S.R. and Hornberger, B. (2017) Time-lapse lab-based x-ray nano-CT study of corrosion damage. *Journal of Microscopy*, **267**, 98–106.
- Brosi, J.K. and Lewandowski, J.J. (2010) Delamination of a sensitized commercial Al–Mg alloy during fatigue crack growth. *Scripta Materialia*, **63**, 799–802. Pergamon.
- Brosi, J.K., Seifi, S.M. and Lewandowski, J.J. (2012) Delamination of sensitized Al-Mg alloy during fatigue crack growth in room temperature air. Pp. 3952–3956 in: *Metallurgical and Materials Transactions A: Physical Metallurgy and Materials Science*.
- Buchheit, R.G. (1995) A Compilation of Corrosion Potentials Reported for Intermetallic Phases in Aluminum Alloys. *Journal of The Electrochemical Society*, **142**, 3994.
- Burnett, T.L., McDonald, S.A., Gholinia, A., Geurts, R., Janus, M., Slater, T., Haigh, S.J., Ornek, C., Almuaili, F., Engelberg, D.L., Thompson, G.E. and Withers, P.J. (2014) Correlative tomography. *Scientific reports*, **4**, 4711. Nature Publishing Group.
- Burnett, T.L., Holroyd, N.J.H., Scamans, G.M., Zhou, X., Thompson, G.E. and Withers, P.J. (2015) The role of crack branching in stress corrosion cracking of aluminium alloys. *Corrosion Reviews*, **33**, 443–454.
- Burnett, T.L., Kelley, R., Winiarski, B., Contreras, L., Daly, M., Gholinia, A., Burke, M.G. and Withers, P.J. (2016) Large volume serial section tomography by Xe Plasma FIB dual beam microscopy. *Ultramicroscopy*, **161**, 119–129. North-Holland.
- Burnett, T.L., Holroyd, N.J.H., Lewandowski, J.J., Ogurreck, M., Rau, C., Kelley, R., Pickering, E.J., Daly, M., Sherry, A.H., Pawar, S., Slater, T.J.A. and Withers, P.J. (2017) Degradation of metallic materials studied by correlative tomography. *IOP Conference Series: Materials Science and Engineering*, **219**, 012001. IOP Publishing.

- Bushfield, H., Cruder, M., Farley, R. and Towers, J. (2003) Marine Aluminum Plate—ASTM Standard Specification B 928 and the Events Leading to Its Adoption. P. in: *October 2003 Meeting of the Society of Naval Architects and Marine Engineers, San Francisco, CA.*
- Carter, S.T., Rotella, J., Agyei, R.F., Xiao, X. and Sangid, M.D. (2018) Measuring fatigue crack deflections via cracking of constituent particles in AA7050 via in situ x-ray synchrotron-based micro-tomography. *International Journal of Fatigue*, **116**, 490–504. Elsevier.
- Connolly, B.J., Horner, D.A., Fox, S.J., Davenport, A.J., Padovani, C., Zhou, S., Turnbull, A., Preuss, M., Stevens, N.P., Marrow, T.J., Buffiere, J.-Y., Boller, E., Groso, A. and Stampanoni, M. (2006) X-ray microtomography studies of localised corrosion and transitions to stress corrosion cracking. *Materials Science and Technology*, **22**, 1076–1085.
- Crane, C.B. and Gangloff, R.P. (2016) Stress corrosion cracking of Al-Mg alloy 5083 sensitized at low temperature. *Corrosion*, **72**, 221–241.
- Crane, C.B., Kelly, R.G. and Gangloff, R.P. (2016) Crack chemistry control of intergranular stress corrosion cracking in sensitized Al-Mg. Pp. 242–263 in: *Corrosion*.
- CT5000 5KN in-situ tensile stage for μ XCT applications | Deben UK – the microscopy accessory experts. (no date) . <[http://deben.co.uk/products/ \$\mu\$ xct-in-situ-holders-testing-stages/tensile-stages-for-x-ray-ct-tomography/](http://deben.co.uk/products/μxct-in-situ-holders-testing-stages/tensile-stages-for-x-ray-ct-tomography/)> (6 August 2018).
- Davenport, A.J., Yuan, Y., Ambat, R., Connolly, B.J., Strangwood, M., Afseth, A. and Scamans, G.M. (2006) Intergranular Corrosion and Stress Corrosion Cracking of Sensitised AA5182. *Materials Science Forum*, **519–521**, 641–646.
- Dix, E.H., Anderson, W.A. and Shumaker, M.B. (1959) Influence of Service Temperature on

- the Resistance of Wrought Aluminum-Magnesium Alloys to Corrosion. *Corrosion*, **15**, 19–26. National Association of Corrosion Engineers.
- Dowd, B.A., Campbell, G.H., Marr, R.B., Nagarkar, V. V., Tipnis, S. V., Axe, L. and Siddons, D.P. (1999) Developments in synchrotron x-ray computed microtomography at the National Synchrotron Light Source. Pp. 224–236 in: (U. Bonse, editor). International Society for Optics and Photonics.
- Eckermann, F., Suter, T., Uggowitzer, P.J., Afseth, A., Davenport, A.J., Connolly, B.J., Larsen, M.H., Carlo, F. De and Schmutz, P. (2008) In situ monitoring of corrosion processes within the bulk of AlMgSi alloys using X-ray microtomography. *Corrosion Science*, **50**, 3455–3466. Pergamon.
- Eckermann, F., Suter, T., Uggowitzer, P.J., Afseth, A., Stampanoni, M., Marone, F. and Schmutz, P. (2009) In Situ Microtomographically Monitored and Electrochemically Controlled Corrosion Initiation and Propagation in AlMgSi Alloy AA6016. *Journal of The Electrochemical Society*, **156**, C1. The Electrochemical Society.
- Gao, W., Wang, D., Seifi, M. and Lewandowski, J.J. (2018) Anisotropy of corrosion and environmental cracking in AA5083-H128 Al-Mg alloy. *Materials Science and Engineering A*, **730**, 367–379. Elsevier.
- Gao, W., Wang, D., Seifi, M. and Lewandowski, J.J. (2019) Through-thickness inhomogeneity of environmentally assisted cracking (EAC) in AA5083-H128 alloy. *Materials Science and Engineering: A*, **740–741**, 34–48. Elsevier.
- Gillen, C., Garner, A., Plowman, A., Race, C.P., Lowe, T., Jones, C., Moore, K.L. and Frankel, P. (2018) Advanced 3D characterisation of iodine induced stress corrosion cracks in zirconium alloys. *Materials Characterization*.

- Goswami, R. and Holtz, R.L. (2013) Transmission Electron Microscopic Investigations of Grain Boundary Beta Phase Precipitation in Al 5083 Aged at 373 K (100 °C). *Metallurgical and Materials Transactions A*.
- Gupta, C., Toda, H., Fujioka, T., Kobayashi, M., Hoshino, H., Uesugi, K., Takeuchi, A. and Suzuki, Y. (2016a) Quantitative tomography of hydrogen precharged and uncharged Al-Zn-Mg-Cu alloy after tensile fracture. *Materials Science and Engineering A*, **670**, 300–313. Elsevier.
- Gupta, C., Toda, H., Fujioka, T., Kobayashi, M., Hoshino, H., Uesugi, K., Takeuchi, A. and Suzuki, Y. (2016b) State of 3-D micro-damage in hydrogen redistributed regions of precharged high strength aluminium alloy. *Corrosion Science*, **111**, 26–38. Pergamon.
- Gürsoy, D., De Carlo, F., Xiao, X. and Jacobsen, C. (2014) TomoPy: A framework for the analysis of synchrotron tomographic data. *Journal of Synchrotron Radiation*, **21**, 1188–1193. International Union of Crystallography.
- Henthorne, M. (2016) The slow strain rate stress corrosion cracking test-a 50 year retrospective. *Corrosion*, **72**, 1488–1518.
- Holroyd, N.J.H. and Scamans, G.M. (2016) Environmental degradation of marine aluminum alloys-Past, present, and future. *Corrosion*, **72**, 136–143. NACE International.
- Holroyd, N.J.H., Evans, J.T. and Scamans, G.M. (2015) Pre-exposure embrittlement of an Al-Cu-Mg alloy, AA2024-T351. *Corrosion Reviews*, **33**, 361–372.
- Holroyd, N.J.H., Burnett, T.L., Seifi, M. and Lewandowski, J.J. (2017a) Improved understanding of environment-induced cracking (EIC) of sensitized 5XXX series aluminium alloys. *Materials Science and Engineering A*, **682**, 613–621.
- Holroyd, N.J.H., Burnett, T.L., Seifi, M. and Lewandowski, J.J. (2017b) Pre-exposure

- embrittlement of a commercial Al-Mg-Mn alloy, AA5083-H131. *Corrosion Reviews*, **35**, 275–290.
- Horner, D.A., Connolly, B.J., Zhou, S., Crocker, L. and Turnbull, A. (2011) Novel images of the evolution of stress corrosion cracks from corrosion pits. *Corrosion Science*, **53**, 3466–3485. Pergamon.
- Jones, R.H. (2003) The influence of hydrogen on the stress-corrosion cracking of low-strength Al-Mg alloys. *Jom*, **55**, 42–46. Springer-Verlag.
- Jones, R.H., Baer, D.R., Danielson, M.J. and Vetrano, J.S. (2001) Role of Mg in the stress corrosion cracking of an Al-Mg alloy. *Metallurgical and Materials Transactions A: Physical Metallurgy and Materials Science*, **32**, 1699–1711. Springer-Verlag.
- Jones, R.H., Gertsman, V.Y., Vetrano, J.S. and Windisch, C.F. (2004) Crack-particle interactions during intergranular stress corrosion of AA5083 as observed by cross-section transmission electron microscopy. *Scripta Materialia*, **50**, 1355–1359. Pergamon.
- Jones, R.H. ((Novacor R.& T.C.. and Danielson, M.J. ((Novacor R.& T.C.. (2003) Role of Hydrogen in Stress Corrosion Cracking of Low-Strength AL-MG Alloys. *Corrosion* **2003**, 1–11.
- Knight, S.P., Salagaras, M., Wythe, A.M., De Carlo, F., Davenport, A.J. and Trueman, A.R. (2010) In situ X-ray tomography of intergranular corrosion of 2024 and 7050 aluminium alloys. *Corrosion Science*, **52**, 3855–3860.
- Knight, S.P., Salagaras, M. and Trueman, A.R. (2011) The study of intergranular corrosion in aircraft aluminium alloys using X-ray tomography. *Corrosion Science*, **53**, 727–734.
- Liu, X., Frankel, G.S., Zoofan, B. and Rokhlin, S.I. (2006a) In Situ X-ray radiographic study of stress corrosion cracking in AA2024-T3. *Corrosion*, **62**, 217–230.

- Liu, X., Frankel, G.S., Zoofan, B. and Rokhlin, S.I. (2006b) Transition from Intergranular Corrosion to Intergranular Stress Corrosion Cracking in AA2024-T3. *Journal of The Electrochemical Society*, **153**, B42. The Electrochemical Society.
- Liu, X., Frankel, G.S., Zoofan, B. and Rokhlin, S.I. (2007) In-situ observation of intergranular stress corrosion cracking in AA2024-T3 under constant load conditions. *Corrosion Science*, **49**, 139–148. Pergamon.
- Oguocha, I.N.A.A., Adigun, O.J. and Yannacopoulos, S. (2008) Effect of sensitization heat treatment on properties of Al-Mg alloy AA5083-H116. *Journal of Materials Science*, **43**, 4208–4214. Springer US.
- Polmear, I. (2006) *Light Alloys: From Traditional Alloys to Nanocrystals*. P. in.: 4th edition. Elsevier Science, 421 pp.
- Rivers, M. (2016) Synchrotron ‘pink beam’ tomography for the study of dynamic processes. *SPIE Newsroom*.
- Scamans, G.M., Holroyd, N.J.H. and Tuck, C.D.S. (1987) The role of magnesium segregation in the intergranular stress corrosion cracking of aluminium alloys. *Corrosion Science*, **27**, 329–347. Pergamon.
- Scotto D’Antuono, D., Gaies, J., Golumbskie, W. and Taheri, M.L. (2014) Grain boundary misorientation dependence of β phase precipitation in an Al-Mg alloy. *Scripta Materialia*, **76**, 81–84. Pergamon.
- Searles, J.L., Gouma, P.I. and Buchheit, R.G. (2001) Stress corrosion cracking of sensitized AA5083 (Al-4.5Mg-1.0Mn). *Metallurgical and Materials Transactions A: Physical Metallurgy and Materials Science*, **32**, 2859–2867. Springer-Verlag.
- Seifi, M., Samimi, P., Ghamarian, I., Collins, P.C. and Lewandowski, J.J. (2015) Grain

- orientation effects on delamination during fatigue of a sensitized Al–Mg alloy. *Philosophical Magazine Letters*, **95**, 526–533.
- Seifi, M., Holroyd, N.J.H. and Lewandowski, J.J. (2016) Deformation rate and sensitization effects on environmentally assisted cracking of Al-Mg naval alloys. Pp. 264–283 in: *Corrosion*.
- Seifi, M., Ghamarian, I., Samimi, P., Collins, P.C., Holroyd, N.J.H. and Lewandowski, J.J. (2018) Sensitization and remediation effects on environmentally assisted cracking of Al-Mg naval alloys. *Corrosion Science*, **138**, 219–241. Pergamon.
- Seong, J., Yang, F., Scheltens, F., Frankel, G.S. and Sridhar, N. (2015) Influence of the Altered Surface Layer on the Corrosion of AA5083. *Journal of the Electrochemical Society*, **162**, C209–C218. The Electrochemical Society.
- Singh, S.S., Williams, J.J., Lin, M.F., Xiao, X., De Carlo, F. and Chawla, N. (2014) In situ investigation of high humidity stress corrosion cracking of 7075 aluminum alloy by three-dimensional (3D) X-ray synchrotron tomography. *Materials Research Letters*, **2**, 217–220. Taylor & Francis.
- Singh, S.S., Williams, J.J., Xiao, X., De Carlo, F. and Chawla, N. (2016a) In situ three dimensional (3D) X-ray synchrotron tomography of corrosion fatigue in Al7075 alloy. Pp. 17–25 in: *Fatigue of Materials II: Advances and Emergences in Understanding*. John Wiley & Sons, Inc., Hoboken, NJ, USA.
- Singh, S.S., Williams, J.J., Xiao, X., De Carlo, F. and Chawla, N. (2016b) In situ three dimensional (3D) X-ray synchrotron tomography of corrosion fatigue in Al7075 alloy. *Fatigue of Materials II: Advances and Emergences in Understanding*, **104**, 17–25.
- Singh, S.S., Williams, J.J., Stannard, T.J., Xiao, X., Carlo, F. De and Chawla, N. (2016c)

- Measurement of localized corrosion rates at inclusion particles in AA7075 by in situ three dimensional (3D) X-ray synchrotron tomography. *Corrosion Science*, **104**, 330–335. Pergamon.
- Singh, S.S., Williams, J.J., Stannard, T.J., Xiao, X., Carlo, F. De and Chawla, N. (2016d) Measurement of localized corrosion rates at inclusion particles in AA7075 by in situ three dimensional (3D) X-ray synchrotron tomography. *Corrosion Science*, **104**, 330–335. Pergamon.
- Singh, S.S., Stannard, T.J., Xiao, X. and Chawla, N. (2017) In Situ X-ray Microtomography of Stress Corrosion Cracking and Corrosion Fatigue in Aluminum Alloys. *Jom*, **69**, 1404–1414.
- Slater, T.J.A., Bradley, R.S., Bertali, G., Geurts, R., Northover, S.M., Burke, M.G., Haigh, S.J., Burnett, T.L. and Withers, P.J. (2017) Multiscale correlative tomography: an investigation of creep cavitation in 316 stainless steel. *Scientific Reports*, **7**, 7332. Nature Publishing Group.
- Staehele, R.W. (2011) Quantitative Micro-Nano (QMN) Approach to SCC Mechanism and Prediction. Pp. 421–424 in: *15th International Conference on Environmental Degradation*. John Wiley & Sons, Inc., Hoboken, New Jersey, Canada.
- Stannard, T.J., Williams, J.J., Singh, S.S., Sundaram Singaravelu, A.S., Xiao, X. and Chawla, N. (2018) 3D time-resolved observations of corrosion and corrosion-fatigue crack initiation and growth in peak-aged Al 7075 using synchrotron X-ray tomography. *Corrosion Science*, **138**, 340–352. Pergamon.
- Tan, L. and Allen, T.R. (2010) Effect of thermomechanical treatment on the corrosion of AA5083. *Corrosion Science*, **52**, 548–554. Pergamon.

- Thermo Fisher Scientific. (2018) Amira-Avizo Software. <<https://www.fei.com/software/amira-avizo/>> (13 January 2019).
- TomoPy — TomoPy 1.1.3 documentation. (no date) . <<https://tomopy.readthedocs.io/en/latest/>> (6 August 2018).
- Turnbull, A. (2014) Corrosion pitting and environmentally assisted small crack growth. *Proceedings of the Royal Society A: Mathematical, Physical and Engineering Sciences*, **470**, 20140254–20140254. The Royal Society.
- Turnbull, A. (2017) Characterising the early stages of crack development in environment-assisted cracking. *Corrosion Engineering Science and Technology*, **52**, 533–540.
- Vallabhaneni, R., Stannard, T.J., Kaira, C.S. and Chawla, N. (2018) 3D X-ray microtomography and mechanical characterization of corrosion-induced damage in 7075 aluminium (Al) alloys. *Corrosion Science*, **139**, 97–113. Pergamon.
- Vargel, C. (2004) *Corrosion of Aluminium*. P. in: *Corrosion of Aluminium*. Elsevier B.V., 1-626 pp.
- WEARMOUTH, W.R., DEAN, G.P. and PARKINS, R.N. (1973) Role of Stress in the Stress Corrosion Cracking of a Mg-Al Alloy. *Corrosion*, **29**, 251–260. National Association of Corrosion Engineers.
- Yang, Y.K. and Allen, T. (2013) Direct visualization of β phase causing intergranular forms of corrosion in Al-Mg alloys. *Materials Characterization*, **80**, 76–85. Elsevier.
- Yuan, Y., Ambat, R., Davenport, A.J., Strangwood, M., Afseth, A. and Scamans, G.M. (2001) Crystallographic effects in intergranular corrosion of an Al-Mg alloy. *Electrochemical Society Proceedings*, **22**, 273–278.
- Zhang, R., Knight, S.P., Holtz, R.L., Goswami, R., Davies, C.H.J. and Birbilis, N. (2016) A

survey of sensitization in 5xxx series aluminum alloys. *Corrosion*, **72**, 144–159.

Zhao, X., Frankel, G.S., Zoofan, B. and Rokhlin, S.I. (2003) In Situ X-Ray Radiographic Study of Intergranular Corrosion in Aluminum Alloys. *Corrosion*, **59**, 1012–1018.